

# Spin drift and diffusion in one- and two-subband helical systems

Gerson J. Ferreira,<sup>1</sup> Felix G. G. Hernandez,<sup>2</sup> Patrick Altmann,<sup>3</sup> and Gian Salis<sup>3</sup>

<sup>1</sup>*Instituto de Física, Universidade Federal de Uberlândia, Uberlândia 38400-902, Minas Gerais, Brazil*

<sup>2</sup>*Instituto de Física, Universidade de São Paulo, São Paulo 05508-090, São Paulo, Brazil*

<sup>3</sup>*IBM Research-Zurich, Säumerstrasse 4, 8803 Rüschlikon, Switzerland*

(Dated: September 1, 2022)

The theory of spin drift and diffusion in two-dimensional electron gases is developed in terms of a random walk model incorporating Rashba, Dresselhaus, and intersubband spin-orbit couplings. The drift velocity breaks the symmetry between parallel and transverse directions, yielding distinct precession patterns near the persistent spin helix (PSH) regime for the single subband case. Moreover, we find that the maximum spin lifetime shifts away from the PSH regime with increasing velocity. We present approximate analytical solutions for these cases and define their domain of validity. Effects of magnetic fields and initial package broadening are also discussed. For systems with two occupied subbands we identify two distinct regimes. For weak intersubband scattering, the sum of the magnetization of independent subbands leads to a chess pattern of crossed PSHs. For strong intersubband scattering, the subbands are averaged and a circular (Bessel) pattern arises. Most of these scenarios were not yet experimentally explored, therefore our results may serve as guidelines for future developments.

## I. INTRODUCTION

The Brownian motion<sup>1,2</sup> provides an elegant description for diffusion processes. A simplified model can be elaborated as a trajectory that consists of successive random steps, where the step size and direction varies according to a given statistical distribution. The extension to spin drift and diffusion<sup>3</sup> of such a random walk model is a powerful tool to describe the spin dynamics in solid state systems. Spin drift and diffusion can also be described in terms of the quasi-classical kinetic equation<sup>4–6</sup> and Monte Carlo simulations<sup>7,8</sup>.

Tuning the spin-orbit couplings (SOC), in a two-dimensional electron gas (2DEG) due to structural (Rashba) and bulk (Dresselhaus) inversion asymmetry is an intensely studied method for the coherent control of the spin dynamics, which is the motivation<sup>9</sup> and one of the central goals of the spintronics research<sup>10–13</sup>. Since the initial proposal of the ballistic spin transistor<sup>9</sup>, generalizations were developed to make it robust against spin-independent scattering<sup>7,14–16</sup>, in order to preserve the spin at a certain orientation.

Persistent spin helix (PSH) states were shown to exhibit long spin lifetimes even in presence of cubic Dresselhaus SOC<sup>8,17–21</sup>. The PSH was first experimentally observed via transient spin-grating spectroscopy<sup>18,22</sup>. Time-resolved Kerr rotation experiments successfully mapped the diffuse dynamics of optically-pumped spin packets<sup>8,23–26</sup> in the PSH regime. Lateral confinement was shown<sup>24,27</sup> to further suppress spin decay by restricting the diffusion to one dimension. The Rashba SOC can be controlled via gate voltages<sup>28,29</sup> to achieve or fine tune the PSH regime<sup>30,31</sup>. Signatures of the PSH regime and measurements of the SOC were also investigated in weak localization measurements<sup>32</sup> and Raman scattering<sup>33</sup>.

In this paper we explore and discuss many interesting scenarios for the spin drift and diffusion based on a generalization of the Brownian motion<sup>1–3</sup>. Starting from an ex-

tension of the random walk (RW) model of Ref. 3, we find new analytical solutions for the single subband case and define their domain of validity. We extend the RW model to incorporate effects of magnetic fields  $\mathbf{B}$  and intersubband SOCs<sup>16,34–39</sup>, considering Rashba ( $\alpha$ ), linear ( $\beta_1$ ) and cubic ( $\beta_3$ ) Dresselhaus cases, as well as their intersubband counterparts<sup>34–40</sup>  $\Gamma$  and  $\eta$ . A finite drift velocity along the  $y \parallel [110]$  direction of a [001] oriented 2DEG in a zincblende semiconductor breaks the symmetry and distinguishes the PSH regimes  $\alpha = \pm(\beta_1 - \beta_3)$ , yielding distinct precession patterns that we label as PSH<sup>+</sup> and PSH<sup>-</sup>, respectively. Additionally, with increasing  $v_d$ , we find that the maximum spin lifetime shifts away from the precise PSH tuning  $\alpha = \pm(\beta_1 - \beta_3)$ . For two-subband systems we identify two possible scenarios. For weak intersubband scattering, the subbands are effectively uncoupled, yielding independent ensembles. The resulting precession pattern is an incoherent sum of the magnetization of the individual subbands, which shows a chess pattern in the crossed PSH regime<sup>39</sup>. For strong intersubband scattering, the subband quantum number becomes a new random variable. The resulting dynamics shows a circular (Bessel) pattern<sup>4</sup>. Overall we organize the results and discussions to serve as guidelines for experimentalists to easily identify and interpret recent<sup>8,24–26</sup> and future developments.

This paper is organized as follows. In Section II we introduce the RW model to establish the notation and identify its main aspects and limitations. Next, in Section III, we discuss in detail the diffusive dynamics for the single subband case. We present analytical approximate solutions valid for a wide range of parameters near the PSH regimes. These are compared with exact numerical solutions. Here we also discuss the expected effects of finite magnetic fields. The two-subband case is discussed in Section IV. We consider a two-subband 2DEG with intraband Rashba and Dresselhaus SOCs, as well as intersubband SOC. We close the paper with general

remarks and the conclusions.

## II. RANDOM WALK FOR SPIN DIFFUSION

The random walk<sup>1–3</sup> (RW) is characterized by the random motion of a particle, which here is an electron that scatters via different processes (e.g., impurity sites, defects, electron-electron scattering, phonons). In between scattering events the electron ballistically travels a distance  $\Delta\mathbf{r} = \mathbf{v}\tau_r$ , where both, the velocity  $\mathbf{v}$  and the scattering time  $\tau_r$ , are random variables. Here,  $\mathbf{v} = v_F\hat{\theta} + \mathbf{v}_d$ , where  $\hat{\theta}$  is an uniformly random direction (along the  $xy$  plane),  $v_F$  is the Fermi velocity, and  $\mathbf{v}_d = \tau e\mathbf{E}/m$  is the drift velocity due to the electric field  $\mathbf{E}$ . Since the scattering events are independent, the scattering time  $\tau_r$  is expected to obey a Poissonian distribution, such that  $\langle\tau_r\rangle = \tau$  and  $\langle\tau_r^2\rangle = 2\tau^2$ .

Throughout the ballistic motion the electron spin precesses due to external magnetic fields or internal velocity-dependent spin-orbit fields. Here we consider  $\tau$  to be short compared with the spin precession period, which allows us to describe below the ballistic spin evolution perturbatively. Considering only non-magnetic scattering, the spin is preserved at each collision, but its precession direction changes due to the SOC. This description leads to a model that is consistent with the Dyakonov-Perel dynamics, which is adequate for typical semiconductors, e.g. GaAs, where this is the dominant mechanism for spin decay.

Let us start with a discrete time dynamics labeled by the step index  $n$ . The position of the electron at the time step  $n+1$  is then  $\mathbf{r}_{n+1} = \mathbf{r}_n + \mathbf{v}_n\tau_n$ . The velocity  $\mathbf{v}_n$  and the time interval  $\tau_n$  depend on the step  $n$  as they are randomized at each collision. During  $\tau_n$  the motion is ballistic and the spin evolution is given as

$$\frac{\partial}{\partial t}\mathbf{s} = \boldsymbol{\Omega} \times \mathbf{s}. \quad (1)$$

Typically, the precession term  $\boldsymbol{\Omega}$  is given by external magnetic fields and the SOCs. But for now let's keep it arbitrary, with the only constraint that the equation above is linear in  $\mathbf{s}$ . An approximate solution for  $|\Omega_n\tau_n| \ll 1$  is obtained iterating the equation above up to second order, yielding

$$\mathbf{s}_{n+1} \approx \mathbf{s}_n + \tau_n \boldsymbol{\Omega}_n \times \mathbf{s}_n + \frac{\tau_n^2}{2} \boldsymbol{\Omega}_n \times (\boldsymbol{\Omega}_n \times \mathbf{s}_n). \quad (2)$$

Here  $\boldsymbol{\Omega}_n \equiv \boldsymbol{\Omega}(\mathbf{v}_n)$  varies in each time step because the SOC depends on  $\mathbf{v}_n$ .

For an ensemble of spins, the magnetization profile  $\mathbf{m}_{n+1}(\mathbf{r})$  at time step  $n+1$  can be written in terms of a joint probability  $P_{n+1}(\mathbf{r}; \mathbf{s})$  of finding an electron at time step  $n+1$  at position  $\mathbf{r}$  having spin  $\mathbf{s}$ ,

$$\mathbf{m}_{n+1}(\mathbf{r}) = \int \mathbf{s} P_{n+1}(\mathbf{r}; \mathbf{s}) d\Sigma, \quad (3)$$

where the integral runs over the Bloch sphere. Since the scattering process is random, the joint probability can be written as the average result of all possible paths from  $n$  to  $n+1$  that lead to an electron at  $\mathbf{r}$  with spin  $\mathbf{s}$ ,

$$P_{n+1}(\mathbf{r}; \mathbf{s}) = \langle P_n(\mathbf{r} - \mathbf{v}_n\tau_n; \mathbf{s} - \Delta\mathbf{s}_n) \rangle, \quad (4)$$

where  $\Delta\mathbf{s}_n = \mathbf{s}_{n+1} - \mathbf{s}_n$ , and  $\langle \dots \rangle$  denotes the average over the momentum direction  $\hat{\theta}$  and the scattering time  $\tau_n$ .

To recover a differential equation for  $\mathbf{m}(\mathbf{r}, t)$ , one expands the average above around  $\langle P_n(\mathbf{r}; \mathbf{s}) \rangle$  up to second order in  $\mathbf{v}_n\tau_n$  and zero order in  $\Delta\mathbf{s}_n$ . Combining all expressions above and converting the discrete time back to the continuum, we get

$$\begin{aligned} \frac{\partial}{\partial t}\mathbf{m}(\mathbf{r}, t) &= \left( \Lambda_{dd} + \Lambda_{pr} \right) \mathbf{m}(\mathbf{r}, t), \\ \Lambda_{dd} &= -\mathbf{v}_d \cdot \nabla + \tau \nabla_v^2, \\ \Lambda_{pr} &= \begin{pmatrix} -\tau \langle \Omega_y^2 \rangle & \tau \langle \Omega_x \Omega_y \rangle & \Xi_y \\ \tau \langle \Omega_x \Omega_y \rangle & -\tau \langle \Omega_x^2 \rangle & -\Xi_x \\ -\Xi_y & \Xi_x & -\tau \langle \Omega_x^2 \rangle - \tau \langle \Omega_y^2 \rangle \end{pmatrix} \end{aligned} \quad (5)$$

where the diagonal term  $\Lambda_{dd}$  drives the drift and diffusion process, while the matrix  $\Lambda_{pr}$  dictates the spin precession and relaxation. The new terms above read

$$\nabla_v^2 = \langle v_x^2 \rangle \partial_x^2 + \langle v_y^2 \rangle \partial_y^2, \quad (6)$$

$$\Xi_x = \langle \Omega_x \rangle - 2\tau \left[ \langle v_x \Omega_x \rangle \partial_x + \langle v_y \Omega_x \rangle \partial_y \right], \quad (7)$$

$$\Xi_y = \langle \Omega_y \rangle - 2\tau \left[ \langle v_x \Omega_y \rangle \partial_x + \langle v_y \Omega_y \rangle \partial_y \right], \quad (8)$$

where we have assumed  $\Omega_z = 0$  for simplicity. This is the case in a [001] oriented 2DEG, where Rashba and Dresselhaus SOC contributions are in-plane. The extra terms for a finite  $\Omega_z$  are shown in Appendix A.

The resulting Eq. (5) differs from those of Ref. 3 as we consider here the Poissonian distribution of the scattering time, such that  $\langle\tau_n\rangle = \tau$  and  $\langle\tau_n^2\rangle = 2\tau$ . Moreover, we keep Eq. (5) in a general form that will allow us to include the external magnetic field and consider two subbands.

### A. Numerical implementation and $\mathbf{q}$ -space

The averages that define Eq. (5) are simple expressions of the system parameters (see next section and the Appendices). Therefore, the only numerical task remaining is to properly solve the initial value problem. Applying a spatial Fourier transform ( $\mathbf{r} \rightarrow \mathbf{q}$ ), the derivatives

become  $\partial_{x/y} \rightarrow -iq_{x/y}$ , and the solution in  $q$ -space is simply

$$\tilde{\mathbf{m}}(\mathbf{q}, t) = e^{\tilde{\Lambda}t} \tilde{\mathbf{m}}(\mathbf{q}, 0), \quad (9)$$

where  $\tilde{\mathbf{m}}(\mathbf{q}, 0)$  is the Fourier transform of the initial packet, and  $\tilde{\Lambda}$  is the Fourier transform of the matrices  $\Lambda_{dd}$  and  $\Lambda_{pr}$  in Eq. (5). Namely,  $\tilde{\Lambda}$  is obtained with the replacements:  $-\mathbf{v}_d \cdot \nabla \rightarrow i\mathbf{v}_d \cdot \mathbf{q}$ ,  $\nabla_v^2 \rightarrow \tilde{\nabla}_v^2 = -(\langle v_x^2 \rangle q_x^2 + \langle v_y^2 \rangle q_y^2)$ , and  $\Xi \rightarrow \tilde{\Xi} = \langle \Omega \rangle + 2i\tau \langle (\mathbf{v} \cdot \mathbf{q}) \Omega \rangle$ . Hereafter we use the symbol  $\sim$  to refer to quantities in  $q$ -space.

The matrix exponential  $e^{\tilde{\Lambda}t}$  can be easily calculated in terms of its eigenvalues and eigenvectors. Therefore, the only relevant numerical<sup>41</sup> task is to perform the two-dimensional inverse Fourier transform ( $\mathbf{q} \rightarrow \mathbf{r}$ ) at different times  $t$  to obtain  $\mathbf{m}(\mathbf{r}, t)$ . Since no extra approximations are involved, we shall consider the numerical evolution as exact solutions of Eq. (5).

## B. Initial broadening

In optical pump-probe experiments, the initial magnetization packet is set by the laser spot, which here is characterized by the initial broadening  $\Gamma_0$ . Therefore, in general we shall consider isotropic Gaussian packets polarized along  $z$ , i.e.  $\mathbf{m}(\mathbf{r}, 0) \propto e^{-\frac{1}{2}(r/\Gamma_0)^2} \hat{z}$ , as the initial condition for Eq. (5). For analytical solutions, we also use initial delta-packets,  $\mathbf{m}(\mathbf{r}, 0) = \delta(\mathbf{r}) \hat{z}$ , which corresponds to the limit  $\Gamma_0 \rightarrow 0$ .

Notice that if we had an exact solution of Eq. (5) for a  $\delta$ -packet, solutions for any other initial shape could be obtained with a convolution. However, the analytical solutions that we discuss in the next sections are approximations. Consequently, a convolution from a  $\delta$  packet solution into a Gaussian might not always be reliable. We'll see next that the approximations used to obtain analytical solutions in the PSH<sup>+</sup> regime are independent of the broadening of the initial packet, therefore one can safely apply a convolution on the initial  $\delta$  packet. In contrast, for the PSH<sup>-</sup> regime we use different approximations for initially narrow ( $\delta$ ) or wide (Gaussian) packets, and we have to treat each case independently.

## III. SINGLE SUBBAND

The spin drift and diffusion in a GaAs quantum well with one subband was experimentally and theoretically discussed in Ref. 25. There, the theoretical model is valid near the PSH<sup>+</sup> regime, i.e.  $\alpha \approx \beta_1 - \beta_3$  for  $\mathbf{v}_d \parallel \hat{y}$ . In this section we reproduce this result using the RW model and show new analytical solutions for the PSH<sup>-</sup> regime  $\alpha \approx -\beta_1 + \beta_3$ . Additionally, we compare the solutions for spatially wide and narrow initial packets. Away from

these limits, we solve the RW model numerically for comparison.

The Hamiltonian for the single subband 2DEG is  $H = \varepsilon_1 + \frac{\hbar^2}{2m} k^2 + \frac{\hbar}{2} \boldsymbol{\sigma} \cdot \boldsymbol{\Omega}$ , where the SOC is given by the Rashba ( $\alpha$ ), linear and cubic Dresselhaus ( $\beta_1$  and  $\beta_3$ ) terms as

$$\boldsymbol{\Omega} = \frac{2}{\hbar} \begin{pmatrix} (+\alpha + \beta_1)k_y + 2\beta_3 \frac{k_x^2 - k_y^2}{k^2} k_y \\ (-\alpha + \beta_1)k_x - 2\beta_3 \frac{k_x^2 - k_y^2}{k^2} k_x \\ 0 \end{pmatrix}. \quad (10)$$

Here  $x \parallel [1\bar{1}0]$  and  $y \parallel [110]$ . Treating the SOC as a weak perturbation to the band structure, the velocity is simply  $\mathbf{v}(\mathbf{k}) = \hbar\mathbf{k}/m$ . Therefore the averages  $\langle \dots \rangle$  over the random motion direction  $\hat{\theta}$  shall be read as an average of  $\mathbf{k}$  over the Fermi circle  $|\mathbf{k}| = k_F$ . Considering the drift velocity  $\mathbf{v}_d = v_d \hat{y}$  we find  $\langle \Omega_y \rangle = \langle \Omega_x \Omega_y \rangle = \langle v_x \Omega_x \rangle = \langle v_y \Omega_y \rangle = 0$ . The other averages remain finite and are shown in Appendix B 1. Within this section we will use the parameters shown in Table I.

TABLE I. Parameters considered for the single subband discussion. The value of the Rashba coefficient  $\alpha$  varies from the PSH<sup>-</sup> to the PSH<sup>+</sup> regime in the range  $-(\beta_1 - \beta_3) \leq \alpha \leq (\beta_1 - \beta_3)$ . The cubic Dresselhaus term near the Fermi level is  $\beta_3 \approx \gamma \pi n_s / 2$ , and  $\gamma = 11 \text{ eV\AA}^3$  is the bulk Dresselhaus coefficient.

Parameter	Value	Description
$m$	$0.067m_0$	Effective mass (GaAs)
$-(\beta_1 - \beta_3) \leq \alpha \leq (\beta_1 - \beta_3)$		Rashba SOC
$\beta_1$	$3.7 \text{ meV\AA}$	Linear Dresselhaus SOC
$\beta_3$	$0.7 \text{ meV\AA}$	Cubic Dresselhaus SOC
$n_s$	$4 \times 10^{11} \text{ cm}^{-2}$	2DEG density
$\tau$	1 ps	Average scattering time

To go forward and find analytical solutions of Eq. (5) we must make approximations. We will consider the PSH<sup>+</sup> ( $\alpha \approx \beta_1 - \beta_3$ ) and PSH<sup>-</sup> ( $\alpha \approx -\beta_1 + \beta_3$ ) regimes. These regimes are different because we keep the drift velocity fixed along  $\hat{y}$ . Equivalently, for a fixed set of SOC coefficients one could alternate between the PSH<sup>±</sup> regimes switching the drift velocity direction<sup>25</sup> between  $\hat{x}$  and  $\hat{y}$ .

### A. PSH<sup>+</sup>: $\alpha \approx \beta_1 - \beta_3$

To establish the approximations for the PSH<sup>+</sup> regime, let us compare the non-diagonal terms  $\tilde{\Xi}_x$  and  $\tilde{\Xi}_y$  in the Fourier space of Eq. (5). The intensity of  $\tilde{\Xi}_x = \langle \Omega_x \rangle + 2i\tau q_y \langle v_y \Omega_x \rangle$  scales with  $(\alpha + \beta_1)$ , while  $\tilde{\Xi}_y = 2i\tau q_x \langle v_x \Omega_y \rangle$  scales with  $(\alpha - \beta_1)$ ; see Appendix B 1. Since our initial packages are always isotropic, the range of  $q_x$  and  $q_y$

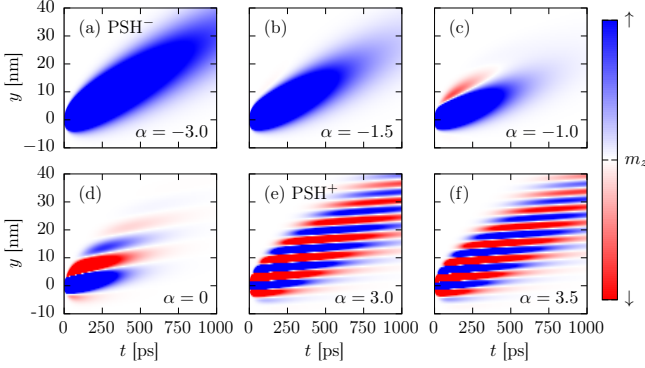


FIG. 1. Transition from PSH<sup>−</sup> to PSH<sup>+</sup> as a function of  $\alpha$  for an initially narrow packet,  $m_z(\mathbf{r}, 0) = \delta(\mathbf{r})$ . Each panel is for a different value of  $\alpha$ , which ranges from the (a) PSH<sup>−</sup> to (e) PSH<sup>+</sup> regime. The labels indicate the value of  $\alpha$  in meVÅ. These and the following images are saturated for better visualization of the magnetization patterns.

are similar, which allow us to approximate both  $|q_x|$  and  $|q_y| \lesssim 1/\Gamma_0$  to compare the intensities of  $\tilde{\Xi}_x$  and  $\tilde{\Xi}_y$ . For  $\alpha \approx \beta_1 - \beta_3$  and  $\beta_3 \ll \alpha + \beta_1$ , we have  $|\tilde{\Xi}_x| \gg |\tilde{\Xi}_y|$ .

We can split the matrix in Eq. (5) in two blocks. A one-dimensional block composed of the  $m_x(\mathbf{r}, t)$  component only, and a two-dimensional block composed of the remaining components,  $m_y(\mathbf{r}, t)$  and  $m_z(\mathbf{r}, t)$ . These blocks are coupled by  $\tilde{\Xi}_y$ . If the difference between eigenvalues of these blocks is large compared to their coupling, one can neglect  $\tilde{\Xi}_y$ . The approximate eigenvalues of the  $yz$  subspace are then

$$\tilde{\lambda}_{yz}^{\pm} \approx \tilde{\lambda}_0 - \tau \left( \langle \Omega_x^2 \rangle + \frac{\langle \Omega_y^2 \rangle}{2} \right) \pm i \tilde{\Xi}_x, \quad (11)$$

where we have used  $|\tau \langle \Omega_y^2 \rangle| \ll |\tilde{\Xi}_x|$ , which follows from the scaling of these quantities with  $(\alpha \pm \beta_1)$ . The eigenvalue of the  $x$  subspace is  $\tilde{\lambda}_x = \tilde{\lambda}_0 - \tau \langle \Omega_y^2 \rangle$ . The common diagonal term  $\tilde{\lambda}_0 = i v_d q_y - \tau \tilde{\nabla}_v^2$  dictates the drift and diffusion. In terms of these eigenvalues, the condition to neglect the coupling  $\tilde{\Xi}_y$  reads  $|\tilde{\lambda}_{yz}^{\pm} - \tilde{\lambda}_x| \gg |\tilde{\Xi}_y|$ . This is satisfied near the PSH<sup>+</sup> regime, but fails near the PSH<sup>−</sup> regime. Therefore we can always neglect  $\tilde{\Xi}_y$  near the PSH<sup>+</sup> regime, and the precession is dominated by the lower block of the matrix in Eq. (5), corresponding to the  $(m_y, m_z)$  subspace. The numerical solutions in Fig. 1 and Fig. 2 show a transition between these two regimes near  $\alpha = -0.7$  meVÅ.

The approximation  $\tilde{\Xi}_y \rightarrow 0$  allows us to write the  $q$ -space solution, Eq. (9), in simple terms and calculate the inverse Fourier transform to obtain the  $z$  component of the magnetization profile, which reads

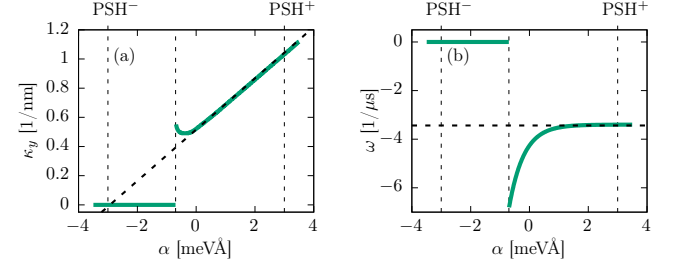


FIG. 2. (a) Wave-number  $\kappa_y$  and (b) frequency  $\omega$  extracted from Fig. 1. For  $\alpha < -0.7$  meVÅ the stripes vanish accompanied by discontinuities in  $\kappa_y$  and  $\omega$ . The PSH<sup>+</sup> solutions given by Eq. (14) and Eq. (15), shown as thick dashed lines, match well the numerical data for  $\alpha > 0$ .

$$m_z^+(\mathbf{r}, t) = \rho(\mathbf{r}, t) e^{-\gamma_p t} \cos(\kappa_y y + \omega t), \quad (12)$$

$$\rho(\mathbf{r}, t) = \frac{1}{\Gamma_{x,t} \Gamma_{y,t}} e^{-\frac{x^2}{2\Gamma_{x,t}^2}} e^{-\frac{(y-v_d t)^2}{2\Gamma_{y,t}^2}} \quad (13)$$

where the broadenings are  $\Gamma_{x,t}^2 = 2Dt$ ,  $\Gamma_{y,t}^2 = 2(D + \tau v_d^2)t$  and the diffusion coefficient is  $D = \tau v_F^2/2$ . The term  $\rho(\mathbf{r}, t)$  drives the drift and diffusion, and it is common to all following solutions discussed hereafter. The wave-vector  $\kappa_y$ , frequency  $\omega$  and relaxation rate  $\gamma_p$  are defined by  $\Omega$ -averages (see Appendix B 2). In terms of the SOC coefficients, up to leading order in  $v_d/v_F$ , these are

$$\kappa_y \approx \frac{2m}{\hbar^2} \left[ \alpha + \beta_1 - \beta_3 - 8\beta_3 \frac{v_d^2}{v_F^2} \right], \quad (14)$$

$$\omega \approx -\frac{2m}{\hbar^2} v_d \beta_3 \left( 1 - 6 \frac{v_d^2}{v_F^2} \right), \quad (15)$$

$$\gamma_p \approx \frac{\tau m^2}{\hbar^4} v_F^2 \left[ 3\beta_3^2 + (\alpha - \beta_1 + \beta_3)^2 - 4 \frac{v_d^2}{v_F^2} (\alpha - \beta_1 - 9\beta_3) \beta_3 \right]. \quad (16)$$

The  $\kappa_y$ ,  $\omega$ ,  $\gamma_p$  and  $D$  above match those of Refs. 25 and 42 for small  $v_d$ . In contrast, our relaxation rate  $\gamma_p$  and diffusion constant  $D$  are twice those of Ref. 3 due to the Poissonian distribution of the scattering time  $\tau_r$  considered here.

The resulting pattern of  $m_z^+(\mathbf{r}, t)$  is shown in Fig. 1(e), where we compare it with the numerical solutions beyond the PSH<sup>±</sup> regimes. The stripes of oscillating spins constitute a magnetization wave moving along  $y$  with velocity  $-\omega/\kappa_y \approx v_d \beta_3/2\beta_1$ , and an envelope profile  $\rho(\mathbf{r}, t)$ . Figure 2 shows that the analytical solution above is valid over a wide range of  $\alpha$  beyond the PSH<sup>+</sup> regime.

Figure 3(a)-(b) shows the decay time  $1/\gamma_p$  as a function of  $\alpha$ , comparing the analytical solution of Eq. (16) with

the numerical simulations for different  $v_d$ . The precise agreement validates the approximations above. With increasing  $v_d$ , the peak of maximum lifetime shifts to larger  $\alpha$  and loses intensity, as seen in Fig. 3(d). This effect is more pronounced for the PSH<sup>−</sup> regime, which we discuss next.

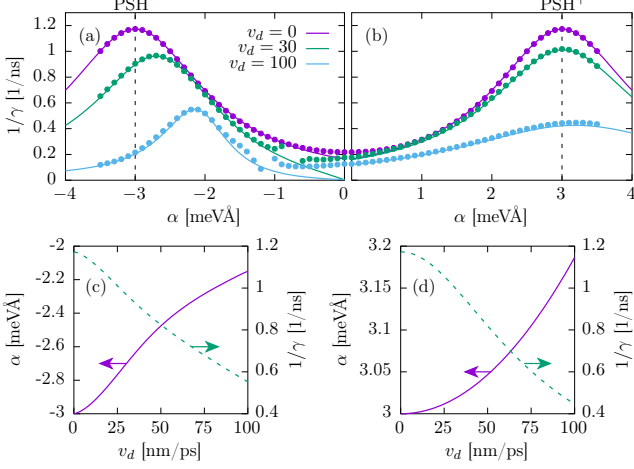


FIG. 3. (a), (b) Decay time  $1/\gamma$  as a function of  $\alpha$  for different  $v_d$  (in nm/ps). The circles were extracted as exponential fits to the numerical solutions in Fig. 1. The analytical solutions (solid lines) match the numerical data for  $\alpha < 0$  using the PSH<sup>−</sup>  $1/\gamma_n$  [Eq. (23)], while for  $\alpha > 0$  it matches the PSH<sup>+</sup>  $1/\gamma_p$  [Eq. (16)]. (c), (d) Peak position ( $\alpha$ ) and intensity ( $1/\gamma$ ) as a function of  $v_d$  for the PSH<sup>±</sup> peaks, respectively.

### B. PSH<sup>−</sup>: $\alpha \approx -\beta_1 + \beta_3$

For the PSH<sup>−</sup> regime,  $\alpha \approx -\beta_1 + \beta_3$ , we get now  $|\tilde{\Xi}_y| \gg |\tilde{\Xi}_x|$ , due to their scaling with  $(\alpha \pm \beta_1)$ . This suggests a splitting of the matrix in Eq. (5) into a  $xz$  block weakly coupled to the  $x$  term by  $\tilde{\Xi}_x$ . However, one can only consider the coupling to be weak if the difference between the eigenvalues of the blocks is much bigger than their coupling. Noticing that  $\langle \Omega_x^2 \rangle \ll \langle \Omega_y^2 \rangle$ , the eigenvalues of the uncoupled blocks ( $\tilde{\Xi}_x = 0$ ) are

$$\tilde{\lambda}_y = \tilde{\lambda}_0 - \tau \langle \Omega_x^2 \rangle, \quad (17)$$

$$\tilde{\lambda}_{xz}^{\pm} \approx \tilde{\lambda}_0 - \tau \langle \Omega_y^2 \rangle \pm i \tilde{\Xi}_y. \quad (18)$$

Therefore, the decoupling condition becomes  $|\tilde{\lambda}_y - \tilde{\lambda}_{xz}^{\pm}| \gg |\tilde{\Xi}_x|$ . As in the PSH<sup>+</sup> regime, the range of  $q_x$  and  $q_y$  is about  $|q_x| = |q_y| \lesssim 1/\Gamma_0$ , which we use to estimate  $\tilde{\Xi}_x$  and  $\tilde{\Xi}_y$ . We find two possible scenarios to satisfy the decoupling: (i) narrow initial packages,  $\Gamma_0 \ll \Gamma_C$ ; and (ii) wide initial packages,  $\Gamma_0 \gg \Gamma_C$ . The critical initial broadening  $\Gamma_C$ , around which the transition occurs, is

$$\Gamma_C \approx \frac{2\langle v_x \Omega_y \rangle}{\langle \Omega_y^2 \rangle} \approx \frac{\hbar^2}{2m\beta_1} \left[ 1 + \frac{\beta_3}{\beta_1} \right]. \quad (19)$$

For the set of parameters used here we find  $\Gamma_C \approx 1.8 \mu\text{m}$ ; see Fig. 4. Next, we discuss the narrow ( $\Gamma_0 \ll \Gamma_C$ ) and wide ( $\Gamma_0 \gg \Gamma_C$ ) initial packet cases separately.

#### 1. Initially narrow packet: $\Gamma_0 \ll \Gamma_C$

For  $\Gamma_0 \ll \Gamma_C$  the precession is set by the  $xz$  block of Eq. (5), since  $|\tilde{\Xi}_y| \propto 1/\Gamma_0$  in  $\tilde{\lambda}_{xz}^{\pm}$  becomes large. Within this subspace, we can solve Eq. (5) analytically to find

$$m_z^-(\mathbf{r}, t) = \rho(\mathbf{r}, t) e^{-\gamma_n t} \cos(\kappa_x x), \quad (20)$$

where  $\rho(\mathbf{r}, t)$  is the same drift-diffusion term from the PSH<sup>+</sup> regime,  $\gamma_n$  is the relaxation rate, and the wave-number  $\kappa_x = \langle v_x \Omega_y \rangle / \langle v_x^2 \rangle$ , which up to leading order in  $v_d/v_F$  reads

$$\kappa_x \approx \frac{2m}{\hbar^2} \left[ -\alpha + \beta_1 - \beta_3 + 2\beta_3 \frac{v_d^2}{v_F^2} \right]. \quad (21)$$

This magnetization profile is shown in Fig. 1(a) as a function of  $y$  and time  $t$  for  $x = 0$  and  $v_d = 30$  nm/ps. In accordance to the equation above, there's no precession along  $y$ .

For typical parameters we find that, although small, the coupling  $\tilde{\Xi}_x \approx \langle \Omega_x \rangle \propto v_d$  has to be included to properly describe  $\gamma_n$  for finite  $v_d$ . We include this coupling into the solution using second order perturbation theory to correct the eigenvalue  $\tilde{\lambda}_{xz}^{\pm} \rightarrow \tilde{\lambda}_{xz}^{\pm} + \delta\tilde{\lambda}_{xz}$ , where

$$\delta\tilde{\lambda}_{xz} \approx \frac{1}{2\tau} \frac{\langle \Omega_x \rangle^2}{\langle \Omega_y^2 \rangle - \langle \Omega_x^2 \rangle}, \quad (22)$$

and the resulting relaxation rate reads

$$\gamma_n \approx \tau \left( \langle \Omega_y^2 \rangle + \frac{\langle \Omega_x^2 \rangle}{2} - \frac{\langle v_x \Omega_y \rangle^2}{\langle v_x^2 \rangle} \right) + \delta\tilde{\lambda}_{xz}, \quad (23)$$

which strongly depends on the drift velocity as shown in Fig. 3(a)-(c). Consequently, its long expression in terms of the SOCs cannot be satisfactorily simplified using series expansions as in the previous solutions. In contrast to the PSH<sup>+</sup> regime, for increasing  $v_d$  the PSH<sup>−</sup> peak of maximum lifetime strongly shifts away from  $\alpha = -(\beta_1 - \beta_3)$ .

#### 2. Initially wide packet: $\Gamma_0 \gg \Gamma_C$

For  $\Gamma_0 \gtrsim \Gamma_C$  we cannot split the matrix in Eq. (5) into simpler blocks. Here, both  $\tilde{\Xi}_x$  and  $\tilde{\Xi}_y$  are relevant. However, a qualitative description can be found in the limit  $\Gamma_0 \rightarrow \infty$ , such that  $\tilde{\Xi}_x \rightarrow \langle \Omega_x \rangle$  and  $\tilde{\Xi}_y \rightarrow 0$ . The precession dynamics is given by the  $yz$  block. Although small,

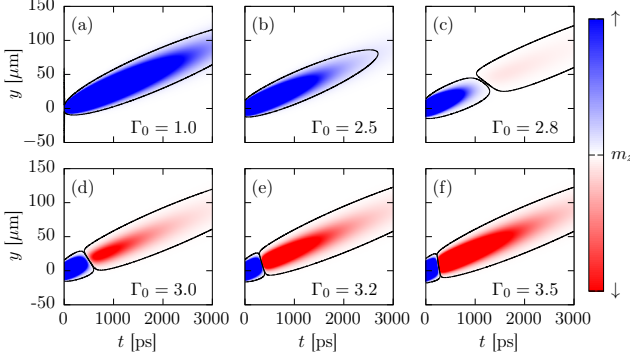


FIG. 4. Magnetization pattern at the PSH<sup>-</sup> regime for initially wide packets for different initial broadenings  $\Gamma_0$ , as indicated in each panel in  $\mu\text{m}$ . Fig. 1(a) corresponds to the  $\Gamma_0 \rightarrow 0$  limit. The spin-flip only occurs for  $\Gamma_0 \gtrsim \Gamma_C \approx 2 \mu\text{m}$ . In panel (a), for  $\Gamma_0 = 1 \mu\text{m}$ , the magnetization fades away for  $t > 3000 \text{ ps}$ , but does not flip, while in panel (b) a node forms around  $t = 3000 \text{ ps}$ . From panel (c) to (f) the transition instant  $t_c$  shifts towards smaller  $t$  with increasing  $\Gamma_0$ . Equation (27) defines  $t_c \approx 100 \text{ ps}$  in the limit  $\Gamma_0 \rightarrow \infty$ . Black line contours are guides to the eye.

the only relevant coupling remaining is  $\tilde{\Xi}_x \approx \langle \Omega_x \rangle \propto v_d$ . Consequently, a small, yet finite drift velocity is required to observe this regime.

Within these approximations, it is easy to solve Eq. (5) in Fourier space and return with the inverse transform to obtain

$$m_z^-(\mathbf{r}, t) = \rho(\mathbf{r}, t) e^{-\gamma_w t} \times \left[ \cosh(\xi t) - \frac{\tau \langle \Omega_y^2 \rangle}{2\xi} \sinh(\xi t) \right]. \quad (24)$$

Here the broadenings in  $\rho(\mathbf{r}, t)$  are approximately constant,  $\Gamma_{x,t} = \Gamma_{y,t} \approx \Gamma_0$ , due to the large initial broadening  $\Gamma_0$ . The relaxation rate  $\gamma_w$  and hyperbolic frequency  $\xi$  are shown in terms of the  $\Omega$ -averages in the Appendix B 3. For  $\alpha \approx -(\beta_1 - \beta_3)$  and up to leading order in  $\beta_3/\beta_1$  and  $v_d/v_F$ ,  $\gamma_w$  and  $\xi$  coincide,

$$\gamma_w \approx \xi \approx \frac{m^2}{\hbar^4} \left[ 4v_F^2 + 8(v_d^2 - v_F^2) \frac{\beta_3}{\beta_1} \right] \tau \beta_1^2. \quad (25)$$

Asymptotically for  $t \rightarrow \infty$ , Eq. (24) becomes  $m_z^-(\mathbf{r}, t) \approx \rho(\mathbf{r}, t) e^{-(\gamma_w - \xi)t} (1 - \frac{\tau \langle \Omega_y^2 \rangle}{2\xi})$ . The factor  $(1 - \frac{\tau \langle \Omega_y^2 \rangle}{2\xi}) < 0$  implies that the magnetization should flip at some instant, as we discuss below. The total relaxation rate in this asymptotic limit becomes

$$\gamma_w - \xi \approx \frac{2m^2}{\hbar^4} (v_F^2 + 18v_d^2) \tau \beta_1^2 + \frac{1}{2\tau} \frac{(v_d \beta_3)^2}{(v_F \beta_1)^2}, \quad (26)$$

which is of the same order as the relaxation rates  $\gamma_n$  and  $\gamma_p$  of the narrow PSH<sup>-</sup>, and PSH<sup>+</sup> regimes, respectively.

The magnetization [see Fig. 4(f)] will have a single nodal line at a time  $t = t_c$  set by the transcendental equation

$$\tanh(\xi t_c) = \frac{2\xi}{\tau \langle \Omega_y^2 \rangle} \approx 1 - \frac{\hbar^4}{8m^2 \tau^2} \frac{(v_d \beta_3)^2}{(v_F \beta_1)^4}, \quad (27)$$

where the approximate value is taken up to leading order in  $v_d/v_F$  and  $\beta_3/\beta_1$ . For  $v_d = 0$  there is no nodal line, i.e.  $t_c \rightarrow \infty$ .

For our set of parameters in Table I and  $v_d = 30 \text{ nm/ps}$  we find  $t_c \approx 115 \text{ ps}$ . However, the analytical solution above is only valid in the limit  $\Gamma_0 \rightarrow \infty$ . More precisely, this limit requires  $|\tilde{\Xi}_x| \gg |\tilde{\Xi}_y|$ , which yields

$$\Gamma_0 \gg \Gamma_W = \frac{2\tau \langle v_x \Omega_y \rangle}{\langle \Omega_x \rangle} \approx 2\tau \frac{v_F^2 \beta_1}{v_d \beta_3}, \quad (28)$$

with  $\Gamma_W \approx 30 \mu\text{m}$ . This is much wider than the typical laser spot used in recent experiments, where  $\Gamma_0$  is  $\sim(\text{sub})\text{micron}$ . Nonetheless, the numerical solutions for  $\Gamma_0$  near the transition from the narrow to the wide PSH<sup>-</sup> regimes are shown in Fig. 4. The single nodal line is already visible for  $\Gamma_0 = \Gamma_C \gtrsim 2 \mu\text{m}$ , while its instant  $t_c$  strongly depends on  $\Gamma_0$ . For  $\Gamma_0 > 30 \mu\text{m}$  the numerical data matches  $t_c = 115 \text{ ps}$  (not shown).

### C. Beyond the PSH regimes and general discussion

To guide our discussion, let's consider a one-subband system similar to the sample discussed in Ref. 25. The relevant parameters are shown in Table I, for which we get the Fermi velocity  $v_F \approx 274 \text{ nm/ps}$ , and the diffusion constant  $D \approx 38 \mu\text{m}^2/\text{ps}$ .

Starting with a  $\delta$  packet,  $m_z(\mathbf{r}, 0) = \delta(\mathbf{r})$ , the numerical drift and diffusion pattern of  $m_z(y, 0)$  at  $x = 0$  is shown in Fig. 1 for  $v_d = 30 \text{ nm/ps}$  and different values of  $\alpha$ . The exact PSH<sup>+</sup> occurs in panel (e), while the exact PSH<sup>-</sup> is shown in panel (a). These match Eq. (12) and Eq. (20), respectively.

For  $\alpha \gtrsim -0.7 \text{ meV\AA}$  the stripes in the magnetization pattern are clearly visible. We can track the node lines to extract the wave-number  $\kappa_y$  and frequency  $\omega$  to compare with the zeros of the cosine in Eq. (12). These are shown in Fig. 2. In the experiment of Ref. 25 the authors measure  $\kappa_y$  and  $\omega$  for a fixed  $\alpha$  near the PSH<sup>+</sup> regime and vary the electric field strength (or  $v_d$ ). The numerical data in Fig. 2 shows that the PSH<sup>+</sup> solutions remain valid for a wide range of  $\alpha$  around the exact PSH<sup>+</sup> regime. Far from the PSH<sup>+</sup> regime, near  $\alpha = -0.7 \text{ meV\AA}$  both  $\kappa_y$  and  $\omega$  diverge as the stripes vanish. In Fig. 2 we calculate  $\kappa_y$  and  $\omega$  only for magnetization maps that have enough nodal lines to establish a periodicity ( $\alpha > -0.7 \text{ meV\AA}$ ), otherwise we set  $\kappa_y = \omega = 0$  ( $\alpha < -0.7 \text{ meV\AA}$ ).

The relaxation rate  $\gamma$  is minimum ( $1/\gamma$  is maximum) at the PSH regimes, as shown in Fig. 3 for  $v_d = 0$ . There

we compare  $\gamma$  extracted from the numerical solutions of Fig. 1 with the analytical expressions of our  $\text{PSH}^\pm$  approximate solutions, Eq. (16) and Eq. (23). For any  $v_d$ , the strength of the  $\text{PSH}^+$  and the  $\text{PSH}^-$  peaks are similar. However, their position shifts away from the  $\text{PSH}^\pm$  conditions, i.e.  $\alpha = \pm(\beta_1 - \beta_3)$ , with increasing  $v_d$ . This new feature is more pronounced for the  $\text{PSH}^-$  regime, and cannot be neglected if one desires to explore this case experimentally.

The magnetization dynamics may strongly depend on the initial broadening  $\Gamma_0$  of the packet, which is set by the laser spot of the pump beam. For the  $\text{PSH}^+$  regime, a wide packet solution can be extracted from the  $\delta$  packet by convolution, as it was done in Ref. 25. In contrast, for initially wide packets, the dynamics of Eq. (24) may dominate in the  $\text{PSH}^-$  regime. Figure 4 shows the transition between the narrow and wide  $\text{PSH}^-$  regimes from the numerical solutions of Eq. (5).

In the narrow  $\text{PSH}^-$  regime ( $\Gamma_0 \ll \Gamma_C$ ) the spin precession is static, given by  $\cos(\kappa_x x)$  in Eq. (20). For  $x = 0$ , the magnetization is constant and one only observes the drift and diffusion process along  $y$ . For  $\Gamma_C < \Gamma_0 < \Gamma_W$ , the system is transitioning from the narrow to the wide regime. Within this range we only have numerical solutions, which qualitatively match the wide  $\text{PSH}^-$  regime ( $\Gamma_0 > \Gamma_W$ ), i.e. the magnetization flips only once. As seen in Fig. 4 for  $\Gamma_0$  within the transition range, the nodal line moves to smaller  $t$  with increasing  $\Gamma_0$ . It matches the wide  $\text{PSH}^-$  regime for  $\Gamma_0 > \Gamma_W \sim 30 \mu\text{m}$  (not shown).

The magnetization flip of the  $\text{PSH}^-$  regime requires a finite drift velocity; see Eq. (27). Here we always consider  $v_d \ll v_F$ , introducing the drift as a small shift of the Fermi circle. For the wide  $\text{PSH}^-$  regime, the drift velocity appears in  $\langle \Omega_x \rangle \propto v_d$  (see Appendix B 3), and affects  $\xi = \frac{1}{2}\sqrt{\tau^2\langle \Omega_y^2 \rangle - 4\langle \Omega_x \rangle^2}$ . For large  $v_d$ , the square-root would become negative and  $\xi$  purely imaginary. This indicates that for large  $v_d$ , the wide  $\text{PSH}^-$  regime would show oscillations and stripes as in the  $\text{PSH}^+$  regime. However, a large  $v_d$  is not consistent with the RW model. Nonetheless, we interpret the single nodal line of the wide  $\text{PSH}^-$  regime as the first node of these speculative drift-induced oscillations.

#### D. External Magnetic Field

Consider the Zeeman term from an in-plane magnetic field  $\mathbf{B} = (B_x, B_y, 0)$ . It adds to the Hamiltonian as  $H_Z = \frac{1}{2}g\mu_B \mathbf{B} \cdot \boldsymbol{\sigma}$ , and complements the spin precession adding  $\boldsymbol{\Omega}_B = g\mu_B \mathbf{B}/\hbar$  to  $\boldsymbol{\Omega}$  in Eq. (10), i.e.  $\boldsymbol{\Omega} \rightarrow \boldsymbol{\Omega} + \boldsymbol{\Omega}_B$ . Here  $g$  is the effective g-factor and  $\mu_B$  is the Bohr magneton. Consequently, the magnetic field yields corrections to the  $\Omega$ -averages in Eq. (5); see Appendix B 4. Particularly, a finite  $B_y$  makes  $\langle \Omega_x \Omega_y \rangle$  and  $\langle v_y \Omega_y \rangle$  finite, while the previous analytical  $\text{PSH}$  solutions require them to be zero. Therefore we shall focus on cases where only the  $B_x$  component is finite, i.e. an in-plane

magnetic field transverse to the drift velocity.

For  $\mathbf{B} = B_x \hat{x}$ , the corrected  $\Omega$ -averages are  $\langle \Omega_x \rangle \rightarrow \langle \Omega_x \rangle + \langle \Delta \Omega_x \rangle$ ,  $\langle \Omega_x^2 \rangle \rightarrow \langle \Omega_x^2 \rangle + \langle \Delta \Omega_x^2 \rangle$ ,  $\langle v_y \Omega_x \rangle \rightarrow \langle v_y \Omega_x \rangle + \langle \Delta v_y \Omega_x \rangle$ , where the corrections are

$$\langle \Delta \Omega_x \rangle = \frac{g\mu_B}{\hbar} B_x, \quad (29)$$

$$\langle \Delta \Omega_x^2 \rangle = \left( \frac{g\mu_B}{\hbar} B_x \right)^2 + \frac{4m}{\hbar^2} \frac{g\mu_B}{\hbar} B_x v_d (\alpha + \beta_1 - 2\beta_3), \quad (30)$$

$$\langle \Delta v_y \Omega_x \rangle = v_d \frac{g\mu_B}{\hbar} B_x. \quad (31)$$

#### 1. $\text{PSH}^+$ and $B_x$

For  $gB_x > 0$ , the  $\Omega$ -average corrections above won't affect the approximations used to get the analytical  $\text{PSH}^+$  solution. But for  $gB_x < 0$ , the corrections will reduce the intensity of  $\tilde{\Xi}_x$ , which may invalidate the condition  $|\tilde{\Xi}_x| \gg |\tilde{\Xi}_y|$ . In general, our  $\text{PSH}^+$  solution will hold for positive  $gB_x$ , and for small negative  $gB_x$  that does not break the inequality. The corrected wave-number  $\kappa_y \rightarrow \kappa_y + \kappa_B$  and frequency  $\omega \rightarrow \omega + \omega_B$  are

$$\kappa_B = \frac{g\mu_B B_x}{\hbar} \cdot \frac{2v_d}{v_F^2 + 2v_d^2} \approx \frac{g\mu_B B_x}{\hbar} \cdot \frac{2v_d}{v_F^2}, \quad (32)$$

$$\omega_B = \frac{g\mu_B B_x}{\hbar} \cdot \frac{v_F^2}{v_F^2 + 2v_d^2} \approx \frac{g\mu_B B_x}{\hbar} \left( 1 - \frac{2v_d^2}{v_F^2} \right). \quad (33)$$

For  $v_d \ll v_F$ , only  $\omega$  is affected by  $B_x$ : the Zeeman frequency simply adds to the frequency of the cubic SOC. This can be understood because in the  $\text{PSH}^+$  situation the effective SOC magnetic field is mostly aligned with  $B_x$ . Therefore,  $B_x$  leads to an additional tilt of the oscillation stripes, which has been used in Ref. 8 to determine the SOC.

#### 2. $\text{PSH}^-$ and $B_x$

In general, for a system near the  $\text{PSH}^-$  regime, a strong  $B_x$  will invalidate the approximations used to obtain analytical solutions. However, a small  $B_x$  can be used to manipulate the nodal line in the single magnetization flip of the wide  $\text{PSH}^-$  regime. The magnetic field adds a term to  $\xi \rightarrow \xi + \xi_B$ , with

$$\begin{aligned} \xi_B \approx & -\frac{\hbar^2}{8m^2} \frac{\beta_1 + 2\beta_3}{\tau v_F^2 \beta_1^3} (g\mu_B B_x)^2 \\ & + \frac{\hbar}{2m} \frac{v_d \beta_3}{\tau v_F^2 \beta_1^2} g\mu_B B_x. \end{aligned} \quad (34)$$

For  $v_d = 0$ , the magnetic correction of  $\xi$  modifies the transcendental equation for  $t_c$  [Eq. (27)], yielding

$$\tanh(\xi t_c) \approx 1 - \frac{\hbar^6}{32m^4\tau^2} \frac{(g\mu_B B_x)^2}{v_F^4 \beta_1^4}. \quad (35)$$

Therefore a small  $B_x$  can play the role of the drift velocity and induce a magnetization flip for the wide PSH<sup>+</sup> regime.

#### IV. TWO SUBBANDS

The inter- and intra-subband SOCs were extensively studied in Refs. 34–39, including a proposal for a crossed persistent spin helix<sup>39</sup> (cPSH) and an intrinsic mechanism for edge spin accumulation<sup>40,43</sup>. In this section we investigate this cPSH within the RW model. The cPSH occurs when the first (second) subband is on the PSH<sup>+</sup> (PSH<sup>-</sup>) regime. The magnetization profile of this crossed regime is not yet explored experimentally.

Here we find two possible scenarios for the two-subband RW model. In the first case, Section IV B, we consider the intersubband scattering (ISS) to be weak, such that the dynamics of the electrons of the first and second subband are independent. The resulting magnetization is an incoherent sum of the magnetization of each subband, and leads to a chess pattern similar to the cPSH of Ref. 39. The second scenario, Section IV C, corresponds to a regime of strong ISS. The random scattering events allow the electrons to quickly visit the Fermi circles of both subbands. In this case each electron feels an average field that now includes an average over the subbands.

Particularly, we will discuss situations where one subband is near the PSH<sup>+</sup> regime, while the other is near the PSH<sup>-</sup>. This can occur in wide quantum wells, where the Hartree repulsion creates effective triangular wells with opposite slopes at each side of the heterostructure<sup>43</sup>. In Ref. 43 the symmetric and antisymmetric wavefunctions are nearly degenerate, allowing a rotation towards wavefunctions located on the left and right triangular wells. Another possibility is to have a slightly asymmetric well, breaking the degeneracy between left and right states.

##### A. Subband and spin precession vectors

The effective Hamiltonian<sup>39</sup> for a two-subband 2DEG with SOC is  $H = H_0 + H_{SOC}$ , with

$$H_0 = \left( \frac{\hbar^2 k^2}{2m} + \varepsilon_+ \right) - \varepsilon_- \lambda_z, \quad (36)$$

$$H_{SOC} = \frac{\hbar}{2} \boldsymbol{\sigma} \cdot [\boldsymbol{\Omega}_+ - \lambda_z \boldsymbol{\Omega}_- + \lambda_x \boldsymbol{\Omega}_{12}], \quad (37)$$

where  $\varepsilon_{\pm} = (\varepsilon_2 \pm \varepsilon_1)/2$  is defined in terms of the first ( $\nu = 1$ ) and second ( $\nu = 2$ ) subband energies  $\varepsilon_{\nu}$ ,  $\boldsymbol{\sigma} = (\sigma_x, \sigma_y, \sigma_z)$  are the spin operators, similarly

$\boldsymbol{\lambda} = (\lambda_x, \lambda_y, \lambda_z)$  act on the subband subspace,  $\boldsymbol{\Omega}_{\pm} = (\boldsymbol{\Omega}_2 \pm \boldsymbol{\Omega}_1)/2$ , and  $m$  is the effective mass.

The spin-orbit fields for each subband  $\nu$  and the intersubband field are

$$\boldsymbol{\Omega}_{\nu} = \frac{2}{\hbar} \begin{pmatrix} (+\alpha_{\nu} + \beta_{1,\nu})k_y + 2\beta_{3,\nu} \frac{k_x^2 - k_y^2}{k^2} k_y \\ (-\alpha_{\nu} + \beta_{1,\nu})k_x - 2\beta_{3,\nu} \frac{k_x^2 - k_y^2}{k^2} k_x \\ 0 \end{pmatrix}, \quad (38)$$

$$\boldsymbol{\Omega}_{12} = \frac{2}{\hbar} \begin{pmatrix} +(\eta - \Gamma)k_y \\ -(\eta + \Gamma)k_x \\ 0 \end{pmatrix}. \quad (39)$$

Here we consider the Rashba  $\alpha_{\nu}$ , linear  $\beta_{1,\nu}$  and cubic  $\beta_{3,\nu}$  Dresselhaus contributions for each subband  $\nu = \{1, 2\}$ , as well as the intersubband SOCs,  $\eta$  and  $\Gamma$ . In general we shall consider  $\boldsymbol{\Omega}_{\nu}$  and  $\boldsymbol{\Omega}_{12}$  as perturbations, such that the energy dispersion remains approximately parabolic near the Fermi level.

The  $\boldsymbol{\Omega}$  vector that defines the spin precession frequency and defines the RW model in Eq. (5) is now

$$\boldsymbol{\Omega} = \boldsymbol{\Omega}_+ - \lambda_z \boldsymbol{\Omega}_- + \lambda_x \boldsymbol{\Omega}_{12}, \quad (40)$$

which is coupled to the subband operators  $\boldsymbol{\lambda}$ . In Section II we have considered the momentum  $\mathbf{k}$  (or  $\hat{\theta}$ ) as a random variable as the electron scatters around the Fermi circle of a subband. Similarly, scattering events may induce subband transitions, allowing us to consider the expectation values of  $\boldsymbol{\lambda}$  as random variables.

Next we assume two possible scenarios regarding the intersubband scattering (ISS) events (e.g. impurity and electron-electron scattering). First, for weak ISS, the subbands can be considered uncoupled, constituting independent ensembles with  $\langle \lambda_z \rangle = \pm 1$ ; see Section IV B. Next, in Section IV C, for strong ISS, the electrons quickly visit all  $k$ -points of both subbands, rendering a random  $\langle \boldsymbol{\lambda} \rangle$ .

##### B. Weak intersubband scattering

The ISS might be weak for large subband splitting  $2\varepsilon_-$  and low temperatures, such that ISS events that require large momentum transfer are suppressed. Therefore, sets of electrons initialized at different subbands constitute independent ensembles with well defined  $\langle \boldsymbol{\lambda} \rangle = (0, 0, \pm 1)$ . Each ensemble follows the dynamics of a single subband, as in Section III.

The total magnetization is then an incoherent sum of the magnetization  $\mathbf{m}_{\nu}(\mathbf{r}, t)$  from each occupied subband,

$$\mathbf{m}(\mathbf{r}, t) = \sum_{\nu} \mathbf{m}_{\nu}(\mathbf{r}, t). \quad (41)$$

### 1. Crossed PSHs

The dynamics of each  $\mathbf{m}_\nu(\mathbf{r}, t)$  depends on the parameters of subband  $\nu$ . A particularly interesting case is when one subband is at the PSH<sup>+</sup> regime and the other is on the PSH<sup>-</sup> regime. This leads to the crossed PSH (cPSH) regime, or Persistent Skyrmion Lattice (PSL), first discussed in Ref. 39.

Consider the parameters from Table II, where subband  $\nu = 1$  is near the PSH<sup>+</sup> regime with  $\alpha_1 \approx \beta_{1,1} - \beta_{3,1}$ , while the other subband  $\bar{\nu} = 2$  is near the PSH<sup>-</sup> regime with  $\alpha_2 \approx -\beta_{1,2} + \beta_{3,2}$ . The z-components of the magnetizations for each subband are

$$m_1(\mathbf{r}, t) = \rho(\mathbf{r}, t) e^{-\gamma_{y,1} t} \cos(\kappa_{y,1} y + \omega_1 t), \quad (42)$$

$$m_2(\mathbf{r}, t) = \rho(\mathbf{r}, t) e^{-\gamma_{x,2} t} \cos(\kappa_{x,2} x). \quad (43)$$

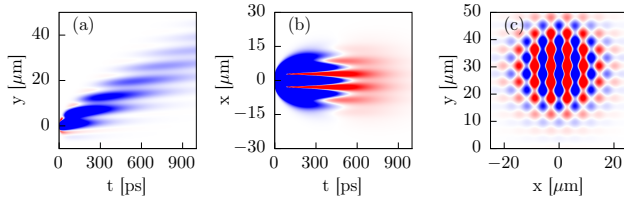


FIG. 5. Magnetization patterns for two-subband crossed PSHs in the weak ISS regime. The first (second) subband is in the PSH<sup>+</sup> (PSH<sup>-</sup>) regime. (a) At  $x = 0$  the magnetization profile is always positive, but show the PSH<sup>+</sup> stripes between zero and finite magnetization. (b) At  $y = 0$  the  $x - t$  map shows a zigzag pattern. (c) Chess pattern<sup>39</sup> at  $t = 1000$  ps centered at  $y = v_d t$ . In panel (b) the colors are highly saturated for better visualization of the pattern.

TABLE II. Parameters considered for the two-subbands system in the weak ISS regime. The intersubband SOC  $\eta$  and  $\Gamma$  are not considered, since, for typical parameters, their contributions are negligible.

Parameter	Value	Description
$m$	$0.067m_0$	Effective mass (GaAs)
$n_s$	$8 \times 10^{11} \text{ cm}^{-2}$	2DEG density
$\varepsilon_g = 2\varepsilon_-$	7 meV	Subband energy difference
$(n_1, n_2)$	$(5.0, 3.0) \times 10^{11} \text{ cm}^{-2}$	Density per subband
$\beta_{1,1} \approx \beta_{1,2}$	3.7 meVÅ	Linear Dresselhaus SOC
$(\beta_{3,1}, \beta_{3,2})$	(0.86, 0.52) meVÅ	Cubic Dresselhaus SOC
$\alpha_1 = -\alpha_2$	3.0 meVÅ	Rashba SOC
$\tau$	1 ps	Average scattering time

The resulting magnetization will have oscillations along  $x$  and  $y$ , yielding the chess pattern of the cPSH; see Fig. 5. For  $x = 0$  the pattern on the  $yt$ -map is approximately given by  $[1 + \cos(\kappa_{y,1} y + \omega_1 t)]$ , which renders the

PSH<sup>+</sup> stripes shifted to positive magnetization. This is a consequence of the incoherent superposition of the PSH<sup>+</sup> of subband  $\nu = 1$ , Eq. (42), and the PSH<sup>-</sup> of subband  $\bar{\nu} = 2$ , Eq. (43), which gives a positive background to the PSH<sup>+</sup> stripes. On the  $xy$ -map for fixed  $t$ , the superposition of oscillations along  $x$  and  $y$  leads to the chess pattern in Fig. 5(c). The drift velocity sets a finite  $\omega_1$ , which leads a motion of the chess pattern with velocity  $v_y = -\omega_1/\kappa_{y,1}$ . However, since the relaxation rates of the PSH<sup>+</sup> and PSH<sup>-</sup> subbands are  $\gamma_{y,1} \neq \gamma_{x,2}$ , for large  $t$  one mode will prevail. In Fig. 5(c) this is seen as slight preference to form stripes rather than the chess pattern at the center of the package.

### 2. Intersubband SOC corrections

Considering the SOC as a perturbation, we use Löwdin perturbation theory to decouple the subbands and obtain an effective precession field  $\Omega_\nu^{\text{eff}}$  for each subband. This is shown in Appendix C. For overall weak SOC, the new terms in  $\Omega_\nu^{\text{eff}}$ , Eq. (C5), do not break the approximations used to obtain the PSH<sup>±</sup> regimes. Consequently, the intersubband SOC introduces corrections to the wave-vectors  $\kappa_{x,\bar{\nu}} \rightarrow \kappa_{x,\bar{\nu}} + \delta\kappa_{x,\bar{\nu}}$ ,  $\kappa_{y,\nu} \rightarrow \kappa_{y,\nu} + \delta\kappa_{y,\nu}$ , and frequency  $\omega_\nu \rightarrow \omega_\nu + \delta\omega_\nu$ . These corrections are expected to be small, since we consider  $\varepsilon_g = 2\varepsilon_- \gg |\hbar\Omega|$ . Up to leading order in  $v_d/v_F$  they read

$$\delta\kappa_{y,\nu} = -\frac{2m^3}{\varepsilon_g^2 \hbar^4} v_{f,\nu}^2 \left[ \eta(-2\Gamma + \eta)\alpha_{\bar{\nu}} - \Gamma(\Gamma - 2\eta)\beta_{1,\bar{\nu}} + (\Gamma - \eta)^2\beta_{3,\bar{\nu}} \right], \quad (44)$$

$$\delta\omega_\nu = -\frac{2m^3 v_F^2 v_d}{\varepsilon_g^2 \hbar^2} \left[ \eta(\eta - 2\Gamma)\alpha_{\bar{\nu}} + \Gamma(\Gamma - 2\eta)\beta_{1,\bar{\nu}} - 2(\Gamma - \eta)^2\beta_{3,\bar{\nu}} \right], \quad (45)$$

$$\delta\kappa_{x,\bar{\nu}} = \frac{2m^3}{\varepsilon_g^2 \hbar^4} v_{f,\bar{\nu}}^2 \left[ \eta(2\Gamma + \eta)\alpha_\nu - \Gamma(\Gamma + 2\eta)\beta_{1,\nu} + (\Gamma + \eta)^2\beta_{3,\nu} \right]. \quad (46)$$

Additionally, the inter-subband SOC will lead to corrections to the relaxation rates ( $\gamma_n$ ,  $\gamma_p$  and  $\gamma_w$ ) and frequency  $\xi$ . However, these are large expressions that we choose not to show explicitly.

### C. Strong intersubband scattering

For strong ISS, scattering events will push the electrons to wander through the Fermi circles of all occupied subbands. Typically, the intersubband scattering time  $\tau_{\text{ISS}}$

is expected to be larger than the intrasubband scattering time  $\tau$ . Therefore, over the ballistic interval  $\tau$ ,  $\langle \lambda \rangle$  is constant. However, for  $\tau_{ISS}$  much shorter than the spin precession period, after some scattering events  $\langle \lambda \rangle$  gets randomized. Since the density of states of a 2DEG is constant and independent of the subband, the expectation values of  $\lambda$  shall be treated as a uniform random variable over a Bloch sphere. The random walk dynamics will be given by Eq. (5) with  $\Omega$  set by Eq. (40), with an average over  $\lambda$  included on the RW averages  $\langle \dots \rangle$ . The new relevant mean values are

$$\langle \lambda_j \rangle = 0, \quad (47)$$

$$\langle \lambda_i \lambda_j \rangle = \frac{1}{3} \delta_{i,j}, \quad (48)$$

where  $i, j = \{x, y, z\}$ , and  $\delta_{i,j}$  is the Kronecker delta.

As in the single subband case, these averages remain exactly zero:  $\langle \Omega_y \rangle = \langle \Omega_x \Omega_y \rangle = \langle v_x \Omega_x \rangle = \langle v_y \Omega_y \rangle = 0$ . The others can be easily calculated algebraically, but now yield long expressions (not shown). Namely, the finite averages are  $\langle \Omega \rangle = \langle \Omega_+ \rangle$ ,  $\langle v_j \Omega \rangle = \langle v_j \Omega_+ \rangle$ ,  $\langle \Omega_j^2 \rangle = \langle \Omega_{+,j}^2 \rangle + \frac{1}{3} \langle \Omega_{-,j}^2 \rangle + \frac{1}{3} \langle \Omega_{12,j}^2 \rangle$ , for  $j = \{x, y\}$ . The spin precession is lead by  $\langle \Omega_+ \rangle$ , which is the average of the intrasubband SOC, while the difference  $\Omega_-$  and the intersubband  $\Omega_{12}$  contribute only to the relaxation. Therefore, apart from  $\Omega_-$  and  $\Omega_{12}$  corrections to the relaxation rate, the resulting dynamics is equivalent to the one of an effective single subband system with effective SOC coefficients  $\alpha_+ = (\alpha_1 + \alpha_2)/2$ ,  $\beta_{1,+} = (\beta_{1,1} + \beta_{1,2})/2$ , and  $\beta_{3,+} = (\beta_{3,1} + \beta_{3,2})/2$ .

TABLE III. Parameters considered for the two-subbands system in the strong ISS regime.

Parameter	Value	Description
$m$	$0.067m_0$	Effective mass (GaAs)
$n_s$	$8 \times 10^{11} \text{ cm}^{-2}$	2DEG density
$\varepsilon_g = 2\varepsilon_-$	$\sim 0 \text{ meV}$	Subband energy difference
$(n_1, n_2)$	$(4.0, 4.0) \times 10^{11} \text{ cm}^{-2}$	Density per subband
$\beta_{1,1} \approx \beta_{1,2}$	$3.7 \text{ meV\AA}$	Linear Dresselhaus SOC
$\beta_{3,1} \approx \beta_{3,2}$	$0.7 \text{ meV\AA}$	Cubic Dresselhaus SOC
$\alpha_1 = -\alpha_2$	$3.0 \text{ meV\AA}$	Rashba SOC
$\eta$	$1 \text{ meV\AA}$	intersubband SOC
$\Gamma$	$1 \text{ meV\AA}$	intersubband SOC
$\tau$	$1 \text{ ps}$	Average scattering time

The strong ISS regime is more likely to occur in systems with small subband energy splitting  $2\varepsilon_-$ . Particularly, if the subbands are in opposite PSH $^\pm$  regimes, with  $\alpha_2 = -\alpha_1$ , one gets  $\alpha_+ = 0$ . Additionally, consider  $\beta_{1,1} = \beta_{1,2}$  and  $\beta_{3,1} = \beta_{3,2}$ , as indicated in Table III. For  $v_d = 0$  the system is isotropic, with  $\Omega$ -averages  $\langle \Omega \rangle = 0$ ,  $\langle v_x \Omega_y \rangle = \langle v_y \Omega_x \rangle$ , and  $\langle \Omega_x^2 \rangle = \langle \Omega_y^2 \rangle$ . This dynamics is

equivalent to the pure Dresselhaus case discussed for a single subband in Ref. 4, where the magnetization follows a Bessel pattern given by

$$m_z(r, t) \propto \frac{e^{-\gamma_0 t}}{\sqrt{t}} J_0(\kappa_0 r), \quad (49)$$

where the wave-number  $\kappa_0$  and the relaxation rate  $\gamma_0$ , up to leading order in  $\beta_{3,+}/\beta_{1,+}$  are

$$\kappa_0 \approx \frac{\sqrt{15} m}{2 \hbar^2} (\beta_{1,+} - \beta_{3,+}), \quad (50)$$

$$\gamma_0 \approx \frac{m^2}{\hbar^4} \tau v_F^2 \frac{7}{8} \left( \beta_{1,+}^2 - 2\beta_{1,+}\beta_{3,+} + \frac{29}{7} \beta_{3,+}^2 \right). \quad (51)$$

These are similar to their PSH $^\pm$  counterparts, i.e. Eqs. (14), (16), (21), (23), in the limit  $\alpha \rightarrow 0$  and  $v_d \rightarrow 0$ . The relaxation rate is dominated by  $\beta_{1,+}^2$ , and, consequently, this state has a much shorter lifetime in comparison with the PSH regimes, where the relaxation goes with  $\beta_3^2$  for  $\alpha \approx \pm(\beta_1 - \beta_3)$ .

For a finite  $v_d$ , the numerical solution in Fig. 6 shows the Bessel pattern distorted by the drift velocity. The numerical pattern at  $t = 1000 \text{ ps}$  shows the Gaussian package centered at  $v_d t = 30 \mu\text{m}$ , while the center of the Bessel pattern is at  $\sim 8 \mu\text{m}$ . Indeed, in the PSH $^+$  regime we have seen that the stripes pattern moves with a velocity  $\approx v_d \beta_3 / 2\beta_1 < v_d$ . Therefore, while we cannot find analytical solutions for this particular case for finite  $v_d$ , it clearly shows mixed features from the Bessel solution above and the PSH $^+$  regime.

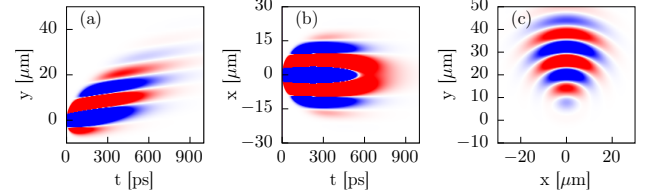


FIG. 6. Magnetization patterns for the two-subbands crossed PSH in the strong coupling limit. (a) On the  $y - t$  map the pattern resembles the stripes of the PSH $^+$  regime. (b) For  $t < 300 \text{ ps}$  the stripes on the  $x - t$  map is similar to the  $\cos(\kappa_x x)$  of the PSH $^-$  regime, but at larger  $t$  features of the circular pattern (c) appears. (c) The magnetization follows a circular pattern on the  $x - y$  plane drifting along  $y$  due to a finite  $v_d$ . Due to the large relaxation rate  $\gamma_0$  of the Bessel solutions, the colors here had to be strongly saturated for clear visualization of the patterns.

## V. FINAL REMARKS AND CONCLUSIONS

### A. Limitations of the Random Walk model

The RW model provides an elegant description of the spin diffusion process. However, there are limitations. To

go from the symbolic definition of the joint probability, Eq. (4), to the differential equation for the magnetization, Eq. (5), we have performed a Taylor expansion for small  $\Delta\mathbf{r} = \mathbf{v}_n\tau$  and  $\Delta\mathbf{s}_n$ . Additionally, we use  $\mathbf{s}_{n+1}$  from Eq. (2) in Eq. (3). We combine these keeping only terms that are linear in  $\mathbf{s}$ , otherwise it is not possible to recover the definition of the magnetization, Eq. (3), and write the differential equation for  $\mathbf{m}(\mathbf{r}, t)$ . As shown here, this approximation is remarkably good for samples with small SOC coefficients, like GaAs quantum wells<sup>25</sup>. However, for strong SOC one cannot neglect the spin-orbit locking that couples the spin with the (Fermi) velocity. This condition would lead to a spin-dependent  $\Delta\mathbf{r}$  (*zitterbewegung*<sup>34,44–46</sup>), thus breaking the conditions required to recover the magnetization in the expansion approach. With a different approach, in Ref. 19 the authors consider the strong SOC regime, and show that the PSH arises from Rabi oscillations. A generalization of the RW model in the lines of the *quantized Hamilton dynamics*<sup>47</sup> may help us overcome these limitations. However, the nonlinearity of the resulting model will surely require numerical solutions.

## B. Conclusions

In conclusion, we have searched for analytical solutions of the RW model for spin diffusion<sup>3</sup> that can be directly applied to experimental measurements<sup>25</sup>. Considering both Rashba and Dresselhaus (linear and cubic) SOCs, we find the drift velocity, induced by an in-plane electric field, breaks the spin diffusion pattern into two distinct regimes,  $\text{PSH}^\pm$ . These are obtained from well defined approximations of the RW model, with a broad range of validity. For the  $\text{PSH}^+$  regime we get the striped magnetization pattern, while for the  $\text{PSH}^-$  we show that no spin-precession is expected at  $x = 0$ , thus explaining a puzzling measurement shown in Ref. 25. Near this  $\text{PSH}^-$

regime, we predict that the diffusion pattern strongly depends on the initial broadening of the spin packet. In both cases ( $\text{PSH}^\pm$ ), the finite drift velocity modifies the relaxation rate, shifting the maximum spin lifetime away from the PSH tuning  $\alpha = \pm(\beta_1 - \beta_3)$ . Additionally, we have extended the RW model to account for effects of a magnetic field (Zeeman term) and two-subbands systems, incorporating the intersubband SOCs as a perturbation. For two-subband systems we have identified two possible scenarios: weak and strong intersubband scattering (ISS). The appropriate scenario will depend on the experimental conditions (temperature, subband energy splitting, scattering sources, etc). For weak ISS, the subbands are effectively uncoupled, and the total magnetization is an incoherent sum of the magnetization of each subband. In this scenario, we find that if the subbands are in the crossed PSH regime, the resulting magnetization shows a chess pattern, in accordance with Ref. 39. For strong ISS, the scattering dynamics yields an average over the subband quantum numbers, which become random in our RW model. The resulting dynamics is that of an effective single-subband system with averaged SOCs. In this case, the crossed PSH regime yields a Bessel pattern, in contrast with the chess pattern obtained in the weak ISS scenario. We expect that our exhaustive search for analytical solutions of the RW model will serve as a valuable tool to guide future experimental developments.

## ACKNOWLEDGMENTS

We acknowledge financial support from the Brazilian agencies CNPq, CAPES and FAPEMIG. G.J.F. thanks Jiyong Fu for helpful discussions. F.G.G.H. acknowledges financial support from grant No. 2014/25981-7 of the São Paulo Research Foundation (FAPESP). P.A. and G.S. acknowledge financial support from the NCCR QSIT of the Swiss National Science Foundation.

---

<sup>1</sup> R. Brown, *Phil. Mag.* **4**, 161 (1828).

<sup>2</sup> A. Einstein, *Ann. Phys.* **322**, 549 (1905).

<sup>3</sup> L. Yang, J. Orenstein, and D.-H. Lee, *Phys. Rev. B* **82**, 155324 (2010).

<sup>4</sup> T. D. Stanescu and V. Galitski, *Phys. Rev. B* **75**, 125307 (2007).

<sup>5</sup> X. Liu and J. Sinova, *Phys. Rev. B* **86**, 174301 (2012).

<sup>6</sup> K. Shen, R. Raimondi, and G. Vignale, *Phys. Rev. B* **90**, 245302 (2014).

<sup>7</sup> M. Ohno and K. Yoh, *Phys. Rev. B* **77**, 045323 (2008).

<sup>8</sup> M. Walser, C. Reichl, W. Wegscheider, and G. Salis, *Nat. Phys.* **8**, 757 (2012).

<sup>9</sup> S. Datta and B. Das, *Appl. Phys. Lett.* **56**, 665 (1990).

<sup>10</sup> S. Wolf, D. Awschalom, R. Buhrman, J. Daughton, S. Von Molnar, M. Roukes, A. Y. Chtchelkanova, and D. Treger, *Science* **294**, 1488 (2001).

<sup>11</sup> I. Žutić, J. Fabian, and S. Das Sarma, *Rev. Mod. Phys.* **76**, 323 (2004).

<sup>12</sup> D. D. Awschalom and M. E. Flatté, *Nat. Phys.* **3**, 153 (2007).

<sup>13</sup> B. Behin-Aein, D. Datta, S. Salahuddin, and S. Datta, *Nat. Nanotechnol.* **5**, 266 (2010).

<sup>14</sup> J. Schliemann, J. C. Egues, and D. Loss, *Phys. Rev. Lett.* **90**, 146801 (2003).

<sup>15</sup> P. Chuang, S.-C. Ho, L. Smith, F. Sfigakis, M. Pepper, C.-H. Chen, J.-C. Fan, J. Griffiths, I. Farrer, H. Beere, *et al.*, *Nat. Nanotechnol.* **10**, 35 (2015).

<sup>16</sup> S. Souma, A. Sawada, H. Chen, Y. Sekine, M. Eto, and T. Koga, *Phys. Rev. Applied* **4**, 034010 (2015).

<sup>17</sup> B. A. Bernevig, J. Orenstein, and S.-C. Zhang, *Phys. Rev. Lett.* **97**, 236601 (2006).

<sup>18</sup> J. D. Koralek, C. Weber, J. Orenstein, B. Bernevig, S.-C. Zhang, S. Mack, and D. Awschalom, *Nature* **458**, 610 (2009).

<sup>19</sup> X. Liu, X.-J. Liu, and J. Sinova, *Phys. Rev. B* **84**, 035318 (2011).

<sup>20</sup> M. C. Lüffe, J. Kailasvuori, and T. S. Nunner, *Phys. Rev. B* **84**, 075326 (2011).

<sup>21</sup> J. Schliemann, [arXiv:1604.02026](https://arxiv.org/abs/1604.02026).

<sup>22</sup> C. P. Weber, J. Orenstein, B. A. Bernevig, S.-C. Zhang, J. Stephens, and D. D. Awschalom, *Phys. Rev. Lett.* **98**, 076604 (2007).

<sup>23</sup> Y. S. Chen, S. Fält, W. Wegscheider, and G. Salis, *Phys. Rev. B* **90**, 121304 (2014).

<sup>24</sup> P. Altmann, M. Kohda, C. Reichl, W. Wegscheider, and G. Salis, *Phys. Rev. B* **92**, 235304 (2015).

<sup>25</sup> P. Altmann, F. G. G. Hernandez, G. J. Ferreira, M. Kohda, C. Reichl, W. Wegscheider, and G. Salis, *Phys. Rev. Lett.* **116**, 196802 (2016).

<sup>26</sup> Y. Kunihashi, H. Sanada, H. Gotoh, K. Onomitsu, M. Kohda, J. Nitta, and T. Sogawa, *Nat. Commun.* **7** (2016).

<sup>27</sup> P. Altmann, M. P. Walser, C. Reichl, W. Wegscheider, and G. Salis, *Phys. Rev. B* **90**, 201306 (2014).

<sup>28</sup> J. Nitta, T. Akazaki, H. Takayanagi, and T. Enoki, *Phys. Rev. Lett.* **78**, 1335 (1997).

<sup>29</sup> M. Studer, G. Salis, K. Ensslin, D. C. Driscoll, and A. C. Gossard, *Phys. Rev. Lett.* **103**, 027201 (2009).

<sup>30</sup> M. Kohda, V. Lechner, Y. Kunihashi, T. Dollinger, P. Olbrich, C. Schönhuber, I. Caspers, V. V. Bel'kov, L. E. Golub, D. Weiss, K. Richter, J. Nitta, and S. D. Ganichev, *Phys. Rev. B* **86**, 081306 (2012).

<sup>31</sup> J. Ishihara, Y. Ohno, and H. Ohno, *Appl. Phys. Express* **7**, 013001 (2013).

<sup>32</sup> A. Sasaki, S. Nonaka, Y. Kunihashi, M. Kohda, T. Bauernfeind, T. Dollinger, K. Richter, and J. Nitta, *Nat. Nanotechnol.* **9**, 703 (2014).

<sup>33</sup> C. Schönhuber, M. P. Walser, G. Salis, C. Reichl, W. Wegscheider, T. Korn, and C. Schüller, *Phys. Rev. B* **89**, 085406 (2014).

<sup>34</sup> E. Bernardes, J. Schliemann, C. Egues, and D. Loss, *Phys. Status Solidi (c)* **3**, 4330 (2006).

<sup>35</sup> E. Bernardes, J. Schliemann, M. Lee, J. C. Egues, and D. Loss, *Phys. Rev. Lett.* **99**, 076603 (2007).

<sup>36</sup> R. S. Calsaverini, E. Bernardes, J. C. Egues, and D. Loss, *Phys. Rev. B* **78**, 155313 (2008).

<sup>37</sup> F. Dettwiler, J. Fu, S. Mack, P. J. Weigle, J. C. Egues, D. D. Awschalom, and D. M. Zumbühl, [arXiv:1403.3518](https://arxiv.org/abs/1403.3518).

<sup>38</sup> J. Fu and J. C. Egues, *Phys. Rev. B* **91**, 075408 (2015).

<sup>39</sup> J. Fu, P. H. Penteado, M. O. Hachiya, D. Loss, and J. C. Egues, [arXiv:1507.00811](https://arxiv.org/abs/1507.00811).

<sup>40</sup> A. Khaetskii and J. C. Egues, [arXiv:1602.00026](https://arxiv.org/abs/1602.00026).

<sup>41</sup> The numerical calculations are developed using the **Julia** language [J. Bezanson, A. Edelman, S. Karpinski, and V. B. Shah, [arXiv:1411.1607](https://arxiv.org/abs/1411.1607)].

<sup>42</sup> G. Salis, M. P. Walser, P. Altmann, C. Reichl, and W. Wegscheider, *Phys. Rev. B* **89**, 045304 (2014).

<sup>43</sup> F. G. G. Hernandez, L. M. Nunes, G. M. Gusev, and A. K. Bakarov, *Phys. Rev. B* **88**, 161305 (2013).

<sup>44</sup> J. Schliemann, D. Loss, and R. M. Westervelt, *Phys. Rev. Lett.* **94**, 206801 (2005).

<sup>45</sup> J. Schliemann, D. Loss, and R. M. Westervelt, *Phys. Rev. B* **73**, 085323 (2006).

<sup>46</sup> J. Schliemann, *Phys. Rev. B* **75**, 045304 (2007).

<sup>47</sup> O. V. Prezhdo and Y. V. Pereverzev, *J. Chem. Phys.* **113**, 6557 (2000).

## Appendix A: Magnetic field along z

In the main text we have assumed  $\Omega_z = 0$  to express Eq. (5) in a simple form. However, a finite  $\Omega_z$  could be introduced by an external magnetic field  $\mathbf{B} = B_z \hat{z}$ , in which case one must add  $W_z$  to the matrices in Eq. (5). Namely

$$W_z = \begin{pmatrix} -\tau\langle\Omega_z^2\rangle & -\Xi_z & +\tau\langle\Omega_x\Omega_z\rangle \\ \Xi_z & -\tau\langle\Omega_z^2\rangle & \tau\langle\Omega_y\Omega_z\rangle \\ \tau\langle\Omega_x\Omega_z\rangle & \tau\langle\Omega_y\Omega_z\rangle & 0 \end{pmatrix}, \quad (\text{A1})$$

where  $\Xi_z = \langle\Omega_z\rangle - 2\tau\left[\langle v_x\Omega_z\rangle\partial_x + \langle v_y\Omega_z\rangle\partial_y\right]$ , and  $\Omega_z = \frac{g\mu_B}{\hbar}B_z$ .

## Appendix B: Expressions for the averages and other secondary quantities mentioned in the text

Here we show large or cumbersome expressions that are not relevant for the main discussion.

### 1. Averages for the single subband case without magnetic field

Here we assume that the drift velocity is along  $\hat{y}$ . The null averages were already mentioned in the main text,  $\langle\Omega_y\rangle = \langle\Omega_x\Omega_y\rangle = \langle v_x\Omega_x\rangle = \langle v_y\Omega_y\rangle = 0$ . The finite ones are

$$\langle v_x^2 \rangle = \frac{1}{2}v_F^2, \quad (\text{B1})$$

$$\langle v_y^2 \rangle = \frac{1}{2}v_F^2 + v_d^2, \quad (\text{B2})$$

$$\langle\Omega_x\rangle = \frac{2m}{\hbar^2}v_d\left(\alpha + \beta_1 - 2\frac{v_d^2 + v_F^2}{v_F^2}\beta_3\right), \quad (\text{B3})$$

$$\begin{aligned} \langle v_y\Omega_x\rangle = \frac{m}{\hbar^2}\left[ & (2v_d^2 + v_F^2)(\alpha + \beta_1) \right. \\ & \left. - \left(v_F^2 + 10v_d^2 + 4\frac{v_d^4}{v_F^2}\right)\beta_3 \right], \end{aligned} \quad (\text{B4})$$

$$\langle v_x\Omega_y\rangle = -\frac{m}{\hbar^2}v_F^2\left(\alpha - \beta_1 + \beta_3 - 2\frac{v_d^2}{v_F^2}\beta_3\right). \quad (\text{B5})$$

The expressions for  $\langle\Omega_x^2\rangle$  and  $\langle\Omega_y^2\rangle$  are large, therefore here we choose to show only their series expansion up to second order in  $v_d/v_F$ ,

#### 4. Complement to the single subband averages due to an external magnetic field

$$\begin{aligned} \langle \Omega_x^2 \rangle &\approx \frac{2m^2 v_F^2}{\hbar^4} \left[ \left( (\alpha + \beta_1)^2 - 2(\alpha + \beta_1)\beta_3 + 2\beta_3^2 \right) \right. \\ &\quad \left. + 2 \frac{v_d^2}{v_F^2} \left( (\alpha + \beta_1)^2 - 10(\alpha + \beta_1)\beta_3 + 18\beta_3^2 \right) \right] \quad (B6) \end{aligned}$$

$$\begin{aligned} \langle \Omega_y^2 \rangle &\approx \frac{2m^2 v_F^2}{\hbar^4} \left[ (\alpha - \beta_1)^2 + 2(\alpha - \beta_1)\beta_3 + 2\beta_3^2 \right. \\ &\quad \left. - \frac{4v_d^2}{v_F^2} (\alpha - \beta_1)\beta_3 \right] \quad (B7) \end{aligned}$$

#### 2. PSH<sup>+</sup>: $\gamma_p$ , $\kappa_y$ and $\omega$

$$\gamma_p = \tau \left( \langle \Omega_x^2 \rangle + \frac{1}{2} \langle \Omega_y^2 \rangle - \frac{\langle v_y \Omega_x \rangle^2}{\langle v_y^2 \rangle} \right), \quad (B8)$$

$$\kappa_y = \frac{\langle v_y \Omega_x \rangle}{\langle v_y^2 \rangle}, \quad (B9)$$

$$\omega = \langle \Omega_x \rangle - \kappa_y v_d \quad (B10)$$

$$\begin{aligned} \langle \Delta \Omega_x \Omega_y \rangle &= \left( \frac{g\mu_B}{\hbar} B_x \right)^2 B_x B_y \\ &\quad + \frac{2m}{\hbar^2} \frac{g\mu_B}{\hbar} B_y v_d (\alpha + \beta_1 - 2\beta_3), \quad (B18) \end{aligned}$$

$$\langle \Delta v_x \Omega \rangle = 0, \quad (B19)$$

$$\langle \Delta v_y \Omega \rangle = v_d \frac{g\mu_B}{\hbar} B. \quad (B20)$$

#### 3. PSH<sup>-</sup>: $\gamma_n$ , and $\kappa_x$

For the narrow initial packet,  $\Gamma_0 \ll \Gamma_C$ :

$$\gamma_n = \tau \left( \langle \Omega_y^2 \rangle + \frac{\langle \Omega_x^2 \rangle}{2} - \frac{\langle v_x \Omega_y \rangle^2}{\langle v_x^2 \rangle} \right) + \frac{1}{2\tau} \frac{\langle \Omega_x \rangle^2}{\langle \Omega_y^2 \rangle - \langle \Omega_x^2 \rangle}, \quad (B11)$$

$$\kappa_x = \frac{\langle v_x \Omega_y \rangle}{\langle v_x^2 \rangle} \quad (B12)$$

For the wide initial packet,  $\Gamma_0 \gg \Gamma_C$ :

$$\gamma_w = \tau \left( \langle \Omega_x^2 \rangle + \frac{1}{2} \langle \Omega_y^2 \rangle \right) \quad (B13)$$

$$\xi = \frac{1}{2} \sqrt{\tau^2 \langle \Omega_y^2 \rangle^2 - 4 \langle \Omega_x \rangle^2} \quad (B14)$$

A finite in-plane magnetic field  $\mathbf{B} = (B_x, B_y, 0)$  introduces additional terms to the  $\Omega$ -averages of Section B 1. Labeling the additive terms of each  $\Omega$ -average with a  $\Delta$ , e.g.  $\langle \Omega \rangle \rightarrow \langle \Omega \rangle + \langle \Delta \Omega \rangle$ , the extra terms due to  $\mathbf{B}$  up to leading order in  $v_d/v_F$  are

$$\langle \Delta \Omega \rangle = \frac{g\mu_B}{\hbar} \mathbf{B}, \quad (B15)$$

$$\langle \Delta \Omega_x^2 \rangle = \left( \frac{g\mu_B}{\hbar} B_x \right)^2 + \frac{4m}{\hbar^2} \frac{g\mu_B}{\hbar} B_x v_d (\alpha + \beta_1 - 2\beta_3), \quad (B16)$$

$$\langle \Delta \Omega_y^2 \rangle = \left( \frac{g\mu_B}{\hbar} B_y \right)^2, \quad (B17)$$

$$\begin{aligned} \langle \Delta v_x \Omega \rangle &= \left( \frac{g\mu_B}{\hbar} B_x \right)^2 B_x B_y \\ &\quad + \frac{2m}{\hbar^2} \frac{g\mu_B}{\hbar} B_y v_d (\alpha + \beta_1 - 2\beta_3), \quad (B18) \end{aligned}$$

$$\langle \Delta v_x \Omega \rangle = 0, \quad (B19)$$

#### Appendix C: Effective model for each subband

To decouple the subbands we use the Löwdin perturbation theory. Consider  $H = H_0 + H'$ , with the perturbation given by the SO term  $H' = H_{SOC}$ . Up to second order in  $(\varepsilon_\nu - \varepsilon_{\bar{\nu}})^{-1}$  we obtain an effective Hamiltonian  $\tilde{H}_\nu$  for each subband  $\nu = \{1, 2\}$ ,

$$\tilde{H}_\nu = \left( \frac{\hbar^2 k^2}{2m} + \varepsilon_\nu \right) + \Delta_\nu^{(2)} + \frac{\hbar}{2} \boldsymbol{\sigma} \cdot (\boldsymbol{\Omega}_\nu + \boldsymbol{\Omega}_\nu^{(3)}), \quad (C1)$$

where  $\Delta_\nu^{(2)}$  is the spin-independent corrections to the subband energy, and  $\boldsymbol{\Omega}_\nu^{(3)} = \Omega_{\nu,x}^{(3)} \hat{x} + \Omega_{\nu,y}^{(3)} \hat{y}$  are the corrections for the effective magnetic field. Using  $\nu$  and  $\bar{\nu}$  to refer to opposite subbands, and taking the approximation  $E \approx \varepsilon_\nu + \hbar^2 k^2 / 2m$ , we get

$$\Delta_\nu^{(2)} = \frac{\left( \hbar \boldsymbol{\Omega}_{12} \right)^2}{4(\varepsilon_\nu - \varepsilon_{\bar{\nu}})}, \quad (C2)$$

$$\Omega_{\nu,y}^{(3)} = \frac{-\hbar^2}{4\varepsilon_g^2} \left[ \Omega_{\bar{\nu},y} [(\Omega_{12,y})^2 - (\Omega_{12,x})^2] + \right. \\ \left. + 2 \Omega_{\bar{\nu},x} \Omega_{12,x} \Omega_{12,y} \right], \quad (C4)$$

where  $\varepsilon_g = \varepsilon_2 - \varepsilon_1$  is the energy difference between the subbands.

This effective model can be used to account for the neglected inter-subband SOC effects in Sections IV B and IV C. For each subband  $\nu$ , the effective precession vector from Eq. (C1) is

$$\Omega_{\nu,x}^{(3)} = \frac{-\hbar^2}{4\varepsilon_g^2} \left[ \Omega_{\bar{\nu},x} [(\Omega_{12,x})^2 - (\Omega_{12,y})^2] + \right. \\ \left. + 2 \Omega_{\bar{\nu},y} \Omega_{12,x} \Omega_{12,y} \right], \quad (C3)$$

$$\boldsymbol{\Omega}_{\nu}^{\text{eff}} = \boldsymbol{\Omega}_{\nu} + \boldsymbol{\Omega}_{\nu}^{(3)}. \quad (C5)$$

Additionally, the subband energy dispersion remains approximately spin-independent,  $E_{\nu} = \varepsilon_{\nu} + \Delta_{\nu}^{(2)} + \hbar^2 k^2 / 2m$ . This assures that the Fermi velocity is isotropic and spin-independent, as required by the RW model of Section II.